Single-Stage PV-Grid Interactive Induction Motor Drive with Improved Flux Estimation Technique for Water Pumping with Reduced Sensors

Saurabh Shukla and Bhim Singh, *Fellow, IEEE*

***Abstract*— This paper deals with a PV-grid integrated system operating an induction motor (IM) coupled to a water pump. A simple DC link voltage regulation approach is adopted for the power transfer. This system is utilized to primarily feed the induction motor-driven water pump and when water pumping is not desired, the power is delivered to the utility. This system requires two current sensors and two voltage sensors in total for sensing and estimation purpose. Induction motor phase currents are estimated from DC link current by modified SVM technique. The speed estimation in this system is achieved by artificial neural network (ANN) based model reference adaptive system (MRAS) with a third order integrator for flux estimation and is capable of controlling the power flow as per demand. The field-oriented control (FOC) is used for speed control of an induction motor (IM)-pump. A third-order integrator based unit voltage generation algorithm is used to control the power transfer in both the direction between utility and the IMD with water pump by regulating DC link voltage. The appropriateness of the system is justified by simulated results on MATLAB/Simulink platform and test results procured with the help of a developed prototype during varying solar irradiances.**

Index Terms*— Solar PV Array, Utility Grid, Voltage Source Inverter (VSI), Field-Oriented Control (FOC), Generalized Integrator, Improved Third Order Integrator (ITOI), P&O Control Algorithm, Induction Motor Drive (IMD), Water Pump, Total Harmonic Distortion (THD), Power Quality.

I. Introduction

THE continuous depletion of conventional energy sources and their adverse impact on the environment are the major cause of all adversity what today's world is facing. In the pursuit of their replacement with renewable energy sources, photovoltaic (PV) power generation is the most popular technology that directly produces electrical power by utilizing solar energy [1].

Conventionally, diesel engine driven water pumps have been extensively used for different purposes in the remote areas. However, nowadays the reliance on PV array operated system has increased. Generally, a PV array fed water pumping system (PVWPS) consists of three sections: solar PV array, DC-DC converter with VSI as power conversion unit, motor and pump assembly. A detailed discussion of generalized structure of high gain DC-DC converters has been reported in [2]. A PV array is the combination of a number of PV modules that are connected in series and parallel. For uninterruptible operations, a battery is linked with the PV array fed water pumping systems to store electrical energy. However, the battery storage requires higher maintenance cost with very less durability [3]. Therefore, to find alternatives to this, plenty of researches have been done. There are some other PVWPSs, where the electric storage (battery) is replaced by water storage tank. There are basically three types of control of an induction motor drive. The conventional speed control technique used for PVWPSs is scalar control.

Saurabh Shukla is with Electrical Engineering Department, Indian Institute of Technology Delhi, New Delhi-110016, India.
(E-mail: saurabh.shukla.ee@gmail.com).

Bhim Singh, *Fellow*, *IEEE* is with the Electrical Engineering Department, Indian Institute of Technology Delhi, New Delhi-110016, India.
(E-mail: bsingh@ee.iitd.ac.in).

However, stability is a major issue and it also suffers from sustained adverse oscillations [4]. Therefore, it is replaced by FOC (field-oriented control) for this application using a reduced number of sensors.

The flux estimation plays a key role in variable frequency drive, controlled by FOC and direct torque control (DTC). The flux estimation by voltage model method is most commonly used since the stator flux is calculated by integrating the back-EMF, which eliminates the mechanical sensor. However, the saturation problem of the pure integral is due to the DC offset in the flux component [5]. Various flux estimation methods have been reported in the literature viz. second order generalized integrator (SOGI) [6], third-order integrator (TOGI) [7] and second-order generalized integrator (SO-SOGI) [8]. The indirect field-oriented control (IFOC) is one of the possible solutions, in which the demerits of open-loop integration can be avoided. In spite of the effectiveness, the problem associated with pure integral is not completely eliminated. This problem can be mitigated by using low pass filter (LPF) up to a certain extent. However, it produces magnitude and phase error especially in the frequency range lower than the cut-off frequency. Therefore, it is mandatory to make the output flux free of all imperfections, which is achieved by a third-order flux integrator.

The mechanical sensorless technique makes the drive feasible for a submersible pump and also curtails the cost. Substantial literature is available on the different sensorless schemes, in which the approach is based on the estimation of improved stator and rotor fluxes for better estimation of motor speed [9]. However, its accuracy is doubtful as it depends upon machine parameters' uncertainty. Despite few saliency-based speed estimation technique e.g. high gain observer (SMO) [10], stochastic filters [11] strategies being a complex and increasing burden on the processor. These are less prone to parameters variation. Another speed estimation technique is parameters adaptation based, with one adjustable model and another reference model, both depend on distinct machine parameters. These MRAS based models are noise immune and simpler. Here back-EMF based MRAS model is used in which the adjustable model depends on the rotor fluxes, which are estimated by a second-order integrator. The output error of the summation of the reference output and adaptive output is processed for speed estimation with the help of voltage controller based on ANN (artificial neural network) [12], which is simple as proportional-integral (PI) controller and is competent to deal with non-linearity and variation in parameters.

The integration of the utility grid and PV array has already been attempted to provide continuous power to the pump to supply water at rated volume [13]. Few of them deal with power feeding the grid with a PV array first and then to the load. This involves a switch connected to the grid. All these aforementioned systems provide the unidirectional power flow either feeding the grid or extracting power from the grid. Attempts have been made to interface the induction motor with the utility grid for power flow

[14]. In the similar manner, permanent magnet synchronous motor (PMSM) [15] and brushless DC motor (BLDC) [16] have been attempted to be interfaced with the grid for delivering power to the load when solar PV power is not sufficient. However, these techniques do not provide the facility to feed the grid when water pumping is not required. The bidirectional control of flow of power is accomplished using a bidirectional converter and the transformer. However, the noisy operation and bulky size, due to the presence of a transformer are a few demerits. An attempt has also been made to integrate two stage PV array with a single phase grid [17] for PMSM drive. However, it requires one DC-DC converter for efficient power transfer from the array to the motor drive, which is costly with more losses in the DC-DC converter [18]. The power flow control of the grid has already been achieved through the unit vector template (UVT) control in [19], which has demerit of notwithstanding the grid distortion condition. Therefore, it is reflected on the voltage component. Therefore, the grid current is also distorted. The existing generalized integrator is incapable of harmonics rejection and has poor DC offset rejection capabilities [20], which affects system performance. Moreover, a generalized integrator has low-pass filters, which creates delay and DC offset and depreciates the system behavior. Hence, an improved third-order integrator is used with added advantages.

The current sensor reduction is nowadays being researched to optimize the cost of the system, as reported in the literature. Few of them are sampling based current reconstruction technique from the DC link current, which suffers from improper sampling due to deficit current information in lower modulation. However, tuned filters are used to solve this problem. Few observer based strategies use prediction of the phase currents in case of less available information [21-22]. The insertion of active voltage vectors, to optimize the time for measuring DC link current, has been reported in [23]. An offset jitter-based technique has been used to cancel the error. In this paper, a modified switching technique is used, which properly reconstructs the phase currents.

The novelty of this system is enlisted as follows,

- The bidirectional power flow capability of the system to work uninterruptedly with the utility grid by solely regulating the DC link voltage.
- For the extraction of fundamental grid voltage component, a technique is used, which is capable to reject harmonics contents and DC offset in single-stage PV fed system.
- Single-stage PV fed system is used here with reduced cost and losses, without a DC-DC converter, where control of motor, DC link voltage regulation and speed are achieved by three-phase VSI.
- The mechanical sensorless control with ANN based MRAS technique having a novel ITOI for flux estimation with DC component elimination capability, is used, which is an almost mandatory requirement for a submersible water pump.
- A wide range speed operation is achieved for a 4-pole 50 Hz IMD with reduced current sensor. Two current sensors, one for DC link current sensing and one for grid current sensing, are used. Moreover, two voltage sensors are sufficient for proper operation.

II. System Architecture

Fig.1 exhibits the configuration of the overall system. It comprises of a 2.2 kW (3 hp), 230 V three-phase IMD. A set of 19 modules and 13 modules are linked in series and parallel, respectively, for modeling of the PV array in MATLAB Simulink. The specifications of PV module used for simulation purpose are given in Appendix A. The cost comparison of this system with the existing similar systems is given in Table III of Appendix E.

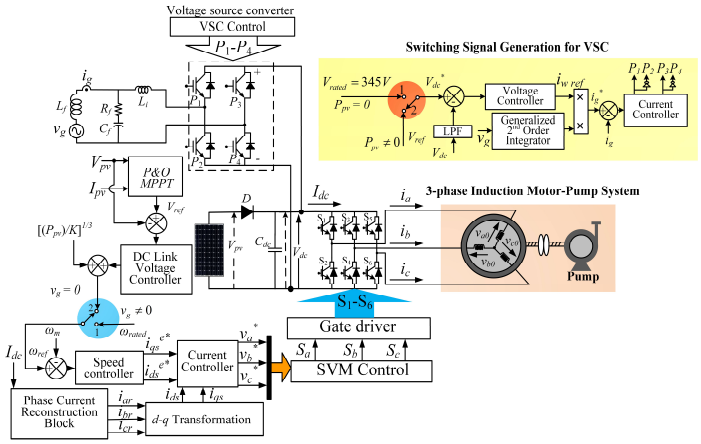

Fig.1 Block diagram of single-stage PV-grid based system

A. Ripple Filter Design

An *R-C* filter is utilized at the grid side utility. It is designed to offer low impedance at the switching frequency component and high impedance at the fundamental frequency component [24].

Therefore, to meet the criteria, $R_fC_f << T_{sw2}$; where C_f, R_f and T_{sw2} are the filter capacitance, resistance and switching time respectively.

Considering $R_fC_f = T_{sw2}/4$, $T_{sw2} = 1/10000$ s and $R_f = 5\ \Omega$, C_f is estimated as,

$$C_f = \frac{T_{sw2}}{4R_f} = \frac{1}{10000 \times 4 \times 5} \cong 5\ \mu F \tag{1}$$

This combination is connected at point of common coupling (PCC) in series.

B. Design of Interfacing Inductor

The selection of an interfacing inductor, L_i depends on the permitted current ripple ΔI_{VSC}. It is estimated as,

$$L_i = \frac{mV_{dc}}{4f_{sav}\Delta I_{VSC}} = \frac{1 \times 345}{4 \times 10000 \times 0.2 \times (2550/345)} = 5.83\ \text{mH} \tag{2}$$

where modulation index, m=1.0, V_{dc}= MPP voltage=345 V, f_{sav}=average switching frequency=10 kHz, and ΔI_{VSC}=20% of I_{VSC}.

III. Motor Current Estimation

This section deals with the current estimation technique by modified SVM technique. The details are given here.

A. Phase Currents Estimation Technique

Table I shows the relationship between line current and DC link current in different sectors. Fig.2 (a) shows that the short active vector at each boundary in every sector, depicted by the shaded area, is incapable of sampling the line current from DC link current. This causes improper sampling. Another reason for this improper sampling is a low modulation index, due to short duration presence of both the active vectors.

The vector sequence is changed from 111 - 110 - 000 - 000 - 110 - 111 to 111 - 110 - 100 - 000 - 000 - 010 - 110 – 111 as shown in Table II.

An averaging technique is used by considering the central point of each switching period T_{sw}, as shown in Fig.2 (b). The equation of the center sampling scheme is obtained as,

$$I^{HA}(t_c)=\frac{I^{H1}(t_{s1})+I^{H2}(t_{s4})}{2},\ I^{LA}(t_c)=-\frac{I^{L1}(t_{s2})+I^{L2}(t_{s3})}{2} \quad (3)$$

where $I^{HA}(t_c)$ and $I^{LA}(t_c)$ are the instantaneous reconstructed motor phase currents, respectively computed at time t_c in the center.

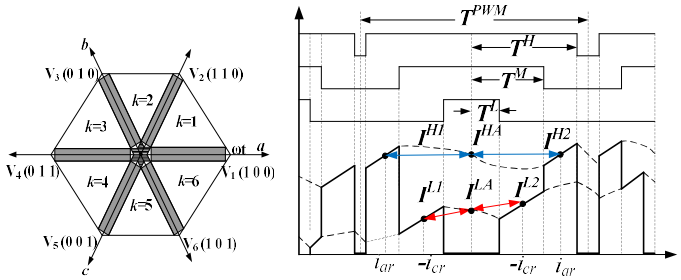

(a) (b)

Fig.2 Current estimation (a) Shaded area showing error region for phase current estimation (b) Averaging scheme

TABLE I VOLTAGE VECTOR RELATION WITH PHASE CURRENT AND DC LINK CURRENT

Sectors (k)	Voltage Vector	Line Currents		
		i_{ar}	i_{br}	i_{cr}
1	$V_1(100)$ $V_2(110)$	I^H	$-(I^H+I^L)$	$-I^L$
2	$V_2(110)$ $V_3(010)$	$-(I^H+I^L)$	I^H	$-I^L$
3	$V_3(010)$ $V_4(011)$	$-I^L$	I^H	$-(I^H+I^L)$
4	$V_4(011)$ $V_5(001)$	$-I^L$	$-(I^H+I^L)$	I^H
5	$V_5(001)$ $V_6(101)$	$-(I^H+I^L)$	$-I^L$	I^H
6	$V_6(101)$ $V_1(100)$	I^H	$-I^L$	$-(I^H+I^L)$

TABLE II PWM OUTPUT SEQUENCE IN MODIFIED CURRENT ESTIMATION APPROACH

Switching sequence ($S_aS_bS_c$)					
Sector I	Sector II	Sector III	Sector IV	Sector V	Sector VI
111	111	111	111	111	111
110 ($-i_{cr}$)	110 ($-i_{cr}$)	011 ($-i_{ar}$)	011 ($-i_{ar}$)	101 ($-i_{br}$)	101 ($-i_{br}$)
100 ($+i_{ar}$)	010 ($+i_{br}$)	010 ($+i_{br}$)	001 ($+i_{cr}$)	001 ($+i_{cr}$)	100 ($+i_{ar}$)
000	000	000	000	000	111
000	000	000	000	000	000
100 ($+i_{ar}$)	010 ($+i_{br}$)	010 ($+i_{br}$)	001 ($+i_{cr}$)	001 ($+i_{cr}$)	100 ($+i_{ar}$)
110 ($-i_{cr}$)	110 ($-i_{cr}$)	011 ($-i_{ar}$)	011 ($-i_{ar}$)	101 ($-i_{br}$)	101 ($-i_{br}$)
111	111	111	111	111	111

IV. SPEED ESTIMATION METHOD

Fig.3 shows the schematic of the sensorless induction motor drive system with speed estimation technique, which is a must for a submersible pump to make it cost-optimized. The adaptive mechanism estimates the speed through back-EMF. In this case, the voltage and current equations are used for reference model, while the same is used with motor speed ω_m to constitute the adjustable model. The governing equations for voltage vector selection in α-β reference frame from switching states are given as,

$$V_{\alpha\beta}=\frac{2}{3}\times V_{dc}\left(S_a+S_b\angle 120+S_c\angle -120\right) \quad (4)$$

The equations for the reference model are given in [25] as,

$$e_d=V_\alpha-R_s i_\alpha-pL_s i_\alpha \quad (5)$$

$$e_q=V_\beta-R_s i_\beta-pL_s i_\beta \quad (6)$$

The adaptive model is given in [21] as,

$$\hat{e}_d=\frac{L_m}{L_r}\times\frac{1}{T_r}\left(L_m i_\alpha-\hat{\psi}_{r\alpha}-\omega_m T_r\hat{\psi}_{r\beta}\right) \quad (7)$$

$$\hat{e}_q=\frac{L_m}{L_r}\times\frac{1}{T_r}\left(L_m i_\beta-\hat{\psi}_{r\beta}+\omega_m T_r\hat{\psi}_{r\alpha}\right) \quad (8)$$

where

$$\hat{\psi}_{r\alpha}=\frac{1}{T_r}\left[\frac{K_1\omega_c^2}{s^3+K_2\omega_c s^2+(K_1+1)\omega_c^2 s+K_2\omega_c^3}\right]\left(L_m i_\alpha-\hat{\psi}_{r\alpha}-\omega_m T_r\hat{\psi}_{r\beta}\right) \quad (9)$$

$$\hat{\psi}_{r\beta}=\frac{1}{T_r}\left[\frac{K_1\omega_c^2}{s^3+K_2\omega_c s^2+(K_1+1)\omega_c^2 s+K_2\omega_c^3}\right]\left(L_m i_\beta-\hat{\psi}_{r\beta}-\omega_m T_r\hat{\psi}_{r\alpha}\right) \quad (10)$$

where $\psi_{r\alpha}$ and $\psi_{r\beta}$ are rotor flux in stationary reference frame, $p=d/dt$ and T_r is the time constant and ω_c is the cut-off frequency.

The rotor flux vector can be calculated by taking Laplace operator. Considering pure integral as flux observer, the observed rotor flux is given in [5] as,

$$\begin{aligned}\psi_r(t)=C_0 t+\frac{C_1}{\omega_1}\sin\left(\omega_1 t+\phi_1-0.5\pi\right)+C_1\frac{\cos\phi_1}{\omega_1}\\+\sum\frac{C_h}{\omega_h}\sin\left(\omega_h t+\phi_h-0.5\pi\right)+\sum C_h\frac{\cos\phi_h}{\omega_h}\end{aligned} \quad (11)$$

Therefore, the DC component $\left(C_1\frac{\cos\phi_1}{\omega_1}+\sum C_h\frac{\cos\phi_h}{\omega_h}\right)$ is always there with linearly increasing trend.

This pure integral can be replaced by LPF$\left(1/\left(s+\omega_c\right)\right)$, when ω_c is the cut-off frequency. Therefore, the estimated flux can be observed as,

$$\begin{aligned}\psi_{r\_LPF}(t)=\frac{C_0}{\omega_c}+\frac{C_0}{\omega_c}e^{-\omega_c t}\\+\sum\frac{C_h}{\sqrt{\omega_h^2+\omega_c^2}}\sin\left(\omega_h t+\phi_h-0.5\pi+\theta_h\right)+\sum C_h\frac{\cos\left(\phi_h+\theta_h\right)}{\sqrt{\omega_h^2+\omega_c^2}}\end{aligned} \quad (12)$$

Therefore, the exponential decay even with the slight DC component, $\left(\sum C_h\frac{\cos\left(\phi_h+\theta_h\right)}{\sqrt{\omega_h^2+\omega_c^2}}\right)$ the saturation effect is removed. However, phase shift, $\theta_h=\arctan\left(\omega_c/\omega_h\right)$ and amplitude attenuation $C_h/\sqrt{\omega_h^2+\omega_c^2}$ are generated by LPF.

Therefore, Fig.4 (a) shows the improved third-order filter $\frac{x_2}{x_1}=\frac{K_1\omega_c^2}{s^3+K_2\omega_c s^2+(K_1+1)\omega_c^2 s+K_2\omega_c^3}$ is used to increase the DC offset rejection capability with harmonic elimination capability. The phase error in the stator flux, which is given as $\left(\theta=\frac{\pi}{2}-\arctan\frac{\omega_c\omega}{\omega_c^2-\omega^2}\right)$, is introduced when the estimated frequency varies from actual frequency of back-EMF. The starting flux offset is alleviated by a constant flux loop as shown in Fig.3. The optimum values of K_1 and K_2 are selected as $\sqrt{2}$ (as the

damping ratio is chosen to be ξ=0.707) and 1.75, respectively for desired dynamic response. It is explained in Appendices.

The speed controller here is neural network controller. The training procedure adopted here is backpropagation method, which tunes the error unless mean square error (MSE) between the output pattern as well as the desired pattern is almost zero [26].

Back-EMF error is processed in ANN block. The input function in terms of back-EMF to the neural network, is given by,

$$v_i = \sum x_i w_i + b = \sum \left(\left(e \times \hat{e} \right) w_i + b \right) \tag{13}$$

The sigmoid activation function is given by,

$$y_i(k) = \frac{e^{\sum \{2 \times ((e \times \hat{e}) w_i + b)\}} - 1}{e^{\sum \{2 \times ((e \times \hat{e}) w_i + b)\}} + 1} \tag{14}$$

This mean square error (MSE) is calculated using following relation,

$$MSE = E(k) = \frac{1}{n} \left[\sum_{i=1}^{n} \left(d_i(k) - \frac{e^{\sum 2^* ((e \times \hat{e}) w_i + b)} - 1}{e^{\sum 2^* ((e \times \hat{e}) w_i + b)} + 1} \right)^2 \right] \tag{15}$$

where for the given input x_i, y_i(k) is the natural response by the network. $d_i(k)$ is the desired response. 'n' is the number of input-output training data and k is the number of iteration. The neuron weights are updated to optimize the value of the cost function MSE. The equation for the weight update is given as,

$$w_{ji}(k+1) = w_{ji}(k) - \xi \frac{\partial E(k)}{\partial w_{ji}(k)} \tag{16}$$

where w_{ji} $(k+1)$ is new weight between i^{th} and j^{th} neurons, w_{ji} (k) is the corresponding old weight, x_i is the output tuning rate.

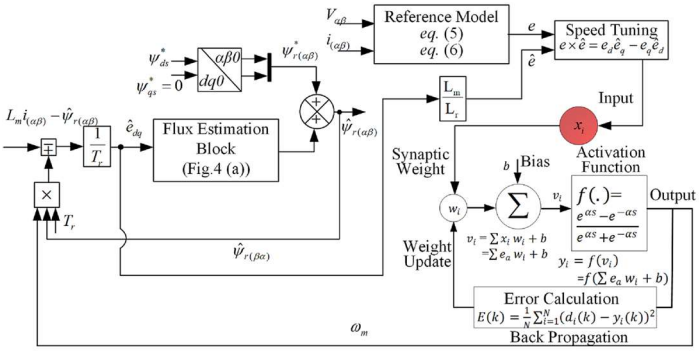

Fig.3 Speed estimation with ANN based back-EMF MRAS

V. Control Mechanism of IMD

Fig.1 presents a schematic of the system. There are two controlling parameters: control for maximum power point tracking and speed control of the motor. These are discussed here.

A. P&O Control Algorithm

This MPPT algorithm deals with the nonlinear relationship of PV array power with PV current and PV voltage. These are discussed in details in [27]. In single-stage topology, maximum power point tracking is controlled by three-phase VSI. There are a number of advantages of single-stage viz. requirement of less circuit components and less expensive. The voltage controller processes the voltage signal (V_{ref} and V_{pv}) and the output is reference speed ω_{ref}.

B. Bidirectional Power Flow Technique

The bidirectional power flow means the power flow can be possible in both the directions in and/or out of the grid. The regulation of the DC link voltage helps in achieving the power flow control, enabling the pump to operate at its rating. Moreover, there should be some provision for power flow to the grid when there is no requirement of pumping. The power flow in both the direction is achieved by the reference DC link voltage V_{dc} compared with DC link voltage. The error signal is processed by a voltage regulator. The output of which is the fundamental current component with the help of the second-order generalized integrator, which has the merits of having improved harmonics and DC offset rejection capabilities in comparison to θ_s component extraction from single-phase PLL as already reported to synchronize the utility voltage and current. The generated reference single-phase current is regulated by hysteresis band-pass controller to generate switching pulses P_1-P_4 for VSC.

Fig.4 (b) exhibits the control for fundamental component extraction through the generalized integrator, which is used to calculate voltage error v_e for eliminating DC offset and it is combined with the utility voltage v_g. The signals at different nodes are given as,

$$v_e = v_g - \frac{K_{dc} \times 2\pi f_g}{s} v_e - v_{gfun}, v_k = K_{sv} v_e - \frac{2\pi f_g}{s} v_{gfun} \tag{17}$$

where f_g=50 Hz, $v_{qv} = \frac{2\pi f_g}{s} v_{gfun}$, $v_{gfun} = \frac{2\pi f_g}{s} v_k$, $v_{dc} = \frac{2\pi f_g}{s} K_{dc} v_e$, K_{dc}=DC-offset gain quantity and K_{sv}=Q-axis gain quantity.

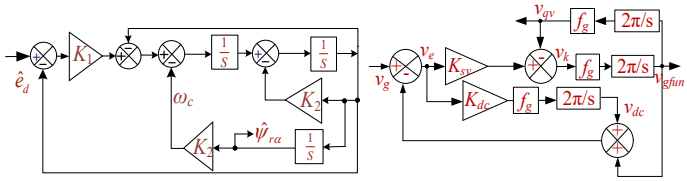

Fig.4 Block diagram (a) flux estimation technique with ITOI (b) fundamental grid voltage extraction using improved method

The transfer functions are derived for each output-to-input v_{gfun}/v_g, v_{dc}/v_g and v_{qv}/v_g as,

$$\frac{v_{gfun}}{v_g} = \frac{s^2 K_{sv} 2\pi f_g}{s^3 + s^2 \left(K_{dc} + K_{sv} \right) 2\pi f_g + s \left(2\pi f_g \right)^2 + \left(2\pi f_g \right)^3 K_{dc}} \tag{18}$$

$$\frac{v_{qv}}{v_g} = \frac{s K_{sv} \left(2\pi f_g \right)^2}{s^3 + s^2 \left(K_{dc} + K_{sv} \right) 2\pi f_g + s \left(2\pi f_g \right)^2 + \left(2\pi f_g \right)^3 K_{dc}} \tag{19}$$

$$\frac{v_{dc}}{v_g} = \frac{K_{dc} \times 2\pi f_g \times \left(s^2 + \left(2\pi f_g \right)^2 \right)}{s^3 + s^2 \left(K_{dc} + K_{sv} \right) 2\pi f_g + s \left(2\pi f_g \right)^2 + \left(2\pi f_g \right)^3 K_{dc}} \tag{20}$$

The condition for system stability is obtained by Routh-Hurwitz stability criterion, in which the tuned value of K_{dc} and K_{sv} are selected in a manner that all Eigen values of characteristic equations should lie on left side of s-plain. Therefore, K_{dc}>0, K_{sv}>0 and 0<K_{dc}<K_{sv}/(2πf_g) are conditions for stability. The value of quadrature component (K_{sv}) is selected as per [28] to get the desired performance. The values of components are given in Appendices.

C. Condition Pertaining to PV Array Feeding Grid

The power is transferred from the PV array to the utility grid, when there is no need of water pumping. The power transfer is also possible, when the panel size is more than the power required for pumping. Fig.5 shows the control technique for the power transfer from a PV array to the grid.

D. Speed Control of Single-Phase PV Grid Based System

The FOC is used for the speed regulation of IMD. The decoupling in torque producing current component of current and excitation current are achieved to make it behave like a DC motor.

The flux-producing current (i_{ds}^*) is calculated as,

$$i_{ds}^* = i_{ds}^{e*} + T_r \times \frac{d}{dt} i_{ds}^{e*} \tag{21}$$

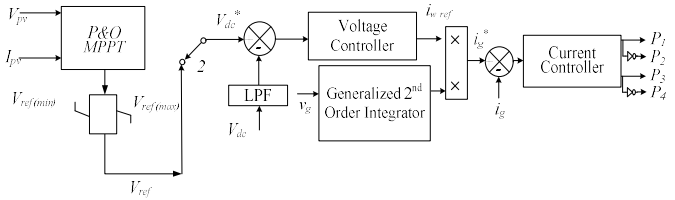

Fig.5 Control diagram of PV array feeding grid

During steady state, the derivative becomes zero in the above equation. The quadrature-axis current (i_{qs}^{e*}) in rotor reference frame is calculated as follows.

When grid is present, ω_{ref} has to be regulated. Hence, selector switch is in position 1 and ω_{ref} is selected as its rated value i.e. ω_{ref}-ω_{rated}. Pertaining to standalone condition, when the grid voltage (v_g) is not available, the switch is shifted to position 2. The output of the voltage regulator is ω_{ref}.

The error signal between the motor speed (ω_m) and reference speed (ω_{ref}) produces motor torque (T_{ek}^*) after being processed by the speed PI controller.

$$T_{e(k)}^* = T_{e(k-1)}^* + K_{p\omega}\left\{\omega_{error(k)} - \omega_{error(k-1)}\right\} + K_{i\omega}\omega_{error(k)} \tag{22}$$

where $\omega_{error} = \omega_{ref} - \omega_m$.

Thus, the torque producing component of the current is given by,

$$i_{qs}^{e*} = T_e^* / \left(K \times i_{ds}^{e*}\right) \tag{23}$$

where $K = 3PL_m / 4L_r$.

The reference synchronous speed (ω_e^*) is calculated as,

$$\omega_e^* = \omega_m + \omega_{sl}^* \tag{24}$$

where $\omega_{sl}^* = i_{qs}^{e*} / \left(T_r \times i_{ds}^{e*}\right)$, is the reference slip speed.

Therefore, for sampling time (T_s), the flux-angle (θ) is given by,

$$\theta_{(k)} = \theta_{(k-1)} + \omega_e^* \times T_s \tag{25}$$

The values of i_{ds} and i_{qs} are obtained by following relations,

$$i_{qs} = i_\beta \cos\theta - i_\alpha \sin\theta \tag{26}$$

$$i_{ds} = i_\beta \sin\theta + i_\alpha \cos\theta \tag{27}$$

where i_α and i_β are the $\alpha\beta 0$ components of the motor phase currents.

These currents are processed with i_{ds}^{e*} and i_{qs}^{e*} and fed to current PI controllers. The output of PI controllers are reference *d-q* voltage signals.

The *d-axis* current error signal is passed through the PI controller which generates *d-axis* voltage as,

$$i_{eds} = i_{ds}^{e*} - i_{ds} \tag{28}$$

$$V_{ds(k)}^* = V_{ds(k-1)}^* + K_{pds}\left\{i_{eds(k)} - i_{eds(k-1)}\right\} + K_{ids} i_{eds(k)} \tag{29}$$

Similarly, *q*-axis voltage is obtained, when the error between the reference and actual *q*-axis current is processed through a PI regulator.

$$i_{eqs} = i_{qs}^{e*} - i_{qs} \tag{30}$$

$$V_{qs(k)}^* = V_{qs(k-1)}^* + K_{pqs}\left\{i_{eqs(k)} - i_{eqs(k-1)}\right\} + K_{iqs} i_{eqs(k)} \tag{31}$$

These obtained voltages with the estimated flux angle (θ) are used to obtain the reference three-phase stationary component of voltages ($V_a^*, V_b^*, \text{and} V_c^*$) as,

$$V_a^* = V_{ds}^* \sin\theta + V_{qs}^* \cos\theta \tag{32}$$

$$V_b^* = V_{ds}^* \sin\left(\theta - 120^o\right) + V_{qs}^* \cos\left(\theta - 120^o\right) \tag{33}$$

$$V_c^* = V_{ds}^* \sin\left(\theta + 120^o\right) + V_{qs}^* \cos\left(\theta + 120^o\right) \tag{34}$$

The resultant voltage (V_R) and the flux angle (θ_k) are computed. The governing equations are given at a particular instant as,

$$V_R = \left[T_u \times v_{s(100)} + T_v \times v_{s(110)}\right] \frac{1}{T_{sw}} \tag{35}$$

$$\left|V_R\right| = \sqrt{\left(V_\alpha^*\right)^2 + \left(V_\beta^*\right)^2}\ ,\ \theta_k = \tan^{-1}\left(V_\beta^* / V_\alpha^*\right) \tag{36}$$

This angle is used for selector determination and switching time allocation for each sector.

where T_u and T_v are 'on' time for (v_s (100)) and (v_s (110)), respectively in sector 1 (Q_1). The time (T_0) corresponds to zero voltage vectors (v_s (000)) and (v_s (111)).

$$T_0 = T_{sw} - T_u - T_v \tag{37}$$

T_u and T_v are calculated as,

$$T_u = \frac{\sqrt{3}}{2}\frac{\left|V_R\right|}{V_{dc}}\left(\cos\theta_k - \frac{1}{\sqrt{3}}\sin\theta_k\right) \times T_{sw}\ \ T_v = \frac{1}{2}\frac{\left|V_R\right|}{V_{dc}}\left(\sqrt{3}\sin\theta_k\right) \times T_{sw} \tag{38}$$

where V_{dc} is the constant DC link voltage at particular insolation level. Therefore, in sector 1 (Q_1), T_u, T_v and T_0 decide the turn-on time for S_1 and S_3 and S_5.

E. Utility Fed System Operation

For a single-stage system, the reference DC link voltage V_{ref} always tries to catch up with MPP voltage (V_{pv}). Therefore, the switch is changed over from the voltage to rated voltage (V_{rated}=345 V), when MPP power (P_{pv}) is zero. The grid is controlled such that when

$$V_{ref} = V_{dc} \text{ if } P_{pv} \neq 0 \text{ and } V_{ref} = 345 \text{ V if } P_{pv} = 0 \tag{39}$$

VI. Simulated Results

This system consisting of a 3-phase, 230 V, 1420 rpm induction motor, PV-grid energized with the peak PV voltage (V_{mp}) of 345 V and PV current (I_{mp}) rating of 6.9 A, is simulated in MATLAB/Simulink environment.

A. Starting Behavior of System

Figs.6 (a-b) present the initial starting system response when operated by a PV array alone. This condition arises at the rated insolation level. The solar PV array alone fulfills the rated power requirements. Because of this reason, the grid current i_g is zero in Fig.6 (b).

Figs.7 (a-b) show similar observation, when the utility grid feeds the pump. This condition occurs during the night or in cloudy weather condition. Smooth starting of the drive is observed even in this operating condition. Grid indices like v_g and i_g are observed in the same phase, as the power is delivered by the grid.

B. Insolation Change: (1000-500) W/m^2

Figs.8 (a-b) exhibit the operation of the motor-pump system. It is observed that PV array delivers the rated power at 1000 W/m^2. This is the reason why the grid current i_g is almost zero. However, as the insolation is decreased to 500 W/m^2, the extra power is drawn from the grid to deliver rated volume of water. Therefore, significant value of the grid current is observed in phase of the grid voltage.

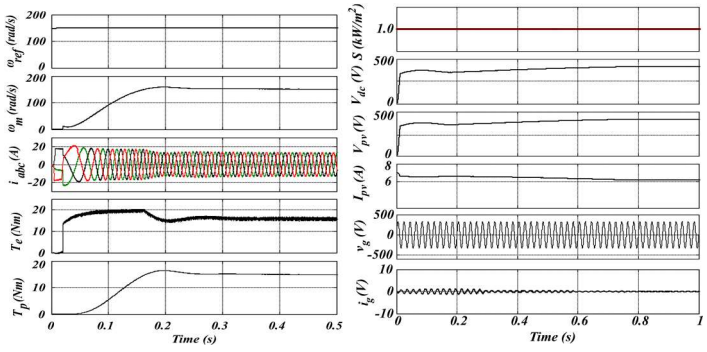

(a) (b)

Fig.6 Starting response for solar PV array fed system (a) IMD (b) PV array and utility grid

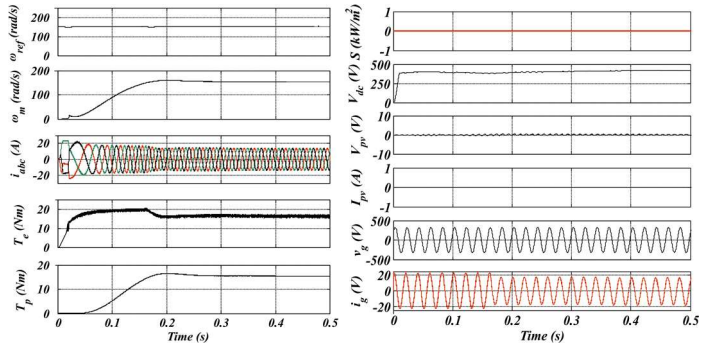

(a) (b)

Fig.7 Starting response of system operated by utility grid (a) IMD indices (b) Solar PV array and utility grid indices

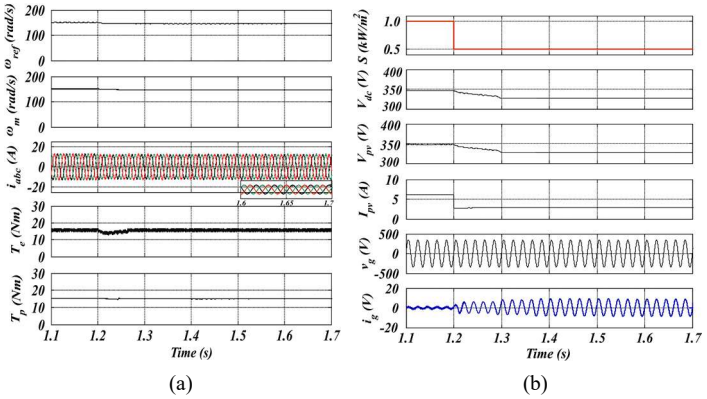

(a) (b)

Fig.8 Step decrement in insolation (1000-500) W/m^2 (a) IMD indices (b) Solar PV array and utility grid indices

C. Insolation Change: (500-1000) W/m^2

Similar observation is made for the drive operating in insolation increment condition. Figs.9 (a-b) exhibit the performance of the motor-pump system. The operation of the drive in both the conditions justify the suitability of the system for wide range of operating condition of insolation change.

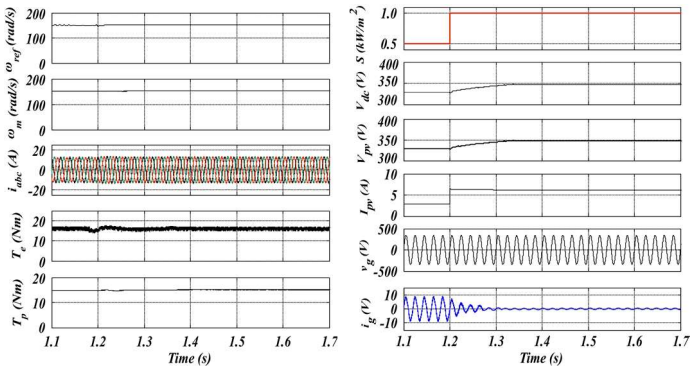

(a) (b)

Fig.9 Step increment in insolation (500-1000) W/m^2 (a) IMD indices (b) Solar PV array and utility grid indices

D. Power Sharing between PV Array and Grid: (1000-500-1000) W/m^2

Fig.10 (a) shows the power sharing between the grid and PV array feeding the motor to operate it at rated condition. It is seen that when insolation is 1000 W/m^2, the power is fed by the PV array alone, whereas it is shared by the grid (P_{grid}), when insolation drops down to 500 W/m^2 at 0.7 s. In either case, the motor is drawing its rated power (P_m). Fig. 10 (b) shows that the THD of the current is well-within the permissible limit imposed by the IEEE-519.

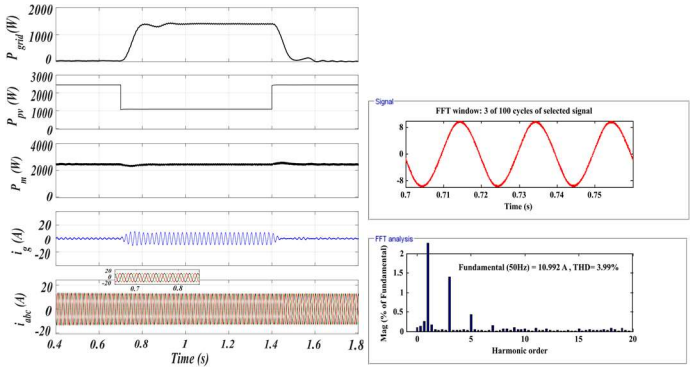

(a) (b)

Fig.10 Simulated waveform (a) power transfer from PV array-grid to motor-pump system during insolation change (1000-500-1000) W/m^2 (b) total harmonic distortion (THD) of grid current at 500 W/m^2 insolation

E. Bode Plots of Flux Adaptation Method with Existing Methods

In terms of DC offset and capability of removing the lower order harmonics, a comparative performance of new flux estimator as compared to the existing techniques is exhibited in Fig.11. It can be observed that the SOGI (blue line) operates poorly in attenuating higher-order harmonics. A comparatively better performance can be observed in the case of SO-SOGI, but it has reluctance in harmonics elimination near the fundamental frequency. This is shown by the Bode plot of the presented third-order integrator (ITOI) (magenta line) that it has better attenuation

capability for lower-order harmonics and for removing DC offset by offering unity gain for 50 Hz component. It can attenuate all lower-order harmonics including fundamental frequencies. As reported in the literature, the transfer functions of SOGI, SO-SOGI, and TOGI are given as $\frac{x_2}{x_1} = \frac{K_1\omega_c}{s^2 + K_1\omega_c s + \omega_c^2}$, $\frac{x_2}{x_1} = \frac{K_1 K_2 \omega_c^3 s}{\left(s^2 + K_2\omega_c s + \omega_c^3\right)\left(s^2 + \omega_c^2\right) + \left(K_1 K_2 + \omega_c^2 s^2\right)}$ and $\frac{x_2}{x_1} = \frac{K_1\omega_c^2 s}{s^3 + \left(K_2 + K_2\right)\omega_c s^2 + \omega_c^2 s + K_1\omega_c^3}$, respectively.

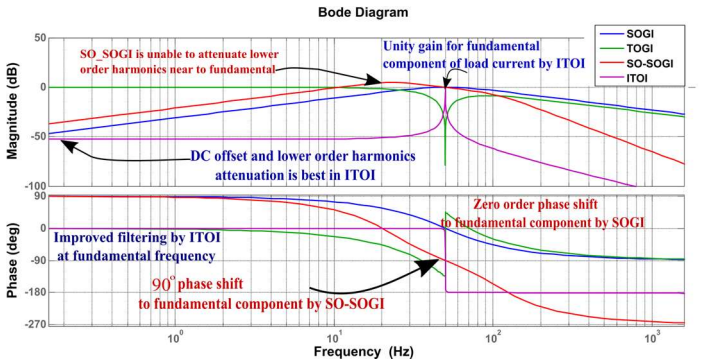

Fig.11 Bode plot of new flux observer in comparison to SOGI, TOGI, SO-SOGI based flux estimation techniques

F. *Bode Plots Pertaining to Integrator Stability*

Fig.12 (a) presents the frequency domain analysis of the new control technique with the existing one. The new integrator has better attenuation capability for higher and lower order frequencies with prominent attenuation of 3rd and 5th order harmonic frequencies.

G. *Utility Grid Distortion Condition*

Fig.12 (b) shows system operation when only the grid feeds the pump. The effect of grid voltage distortion and DC offset is eliminated by this control (explained in the previous section), which is quite frequent in the distribution network. For this purpose, the higher-order harmonics (3rd and 5th) are introduced in the grid voltage and the analysis is done. The reflected harmonics on the grid current can be seen in the figure with conventional control (UVT and GI) as well as with this new algorithm.

VII. Hardware Validation

Fig.13 shows a prototype developed in the laboratory, which includes a PV simulator (AMETEK make ETS600x17DPVF TerraSAS). Two VSCs 600/415–35F (SEMIKRON MD B6CI) are used. Four Hall Effect sensors are used for sensing voltages and currents. A DSP (dSPACE-1202) is utilized for signal processing and control.

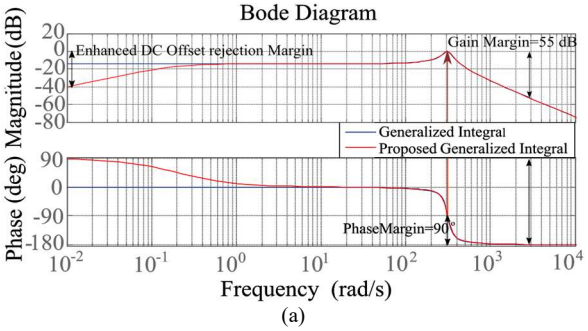

(a)

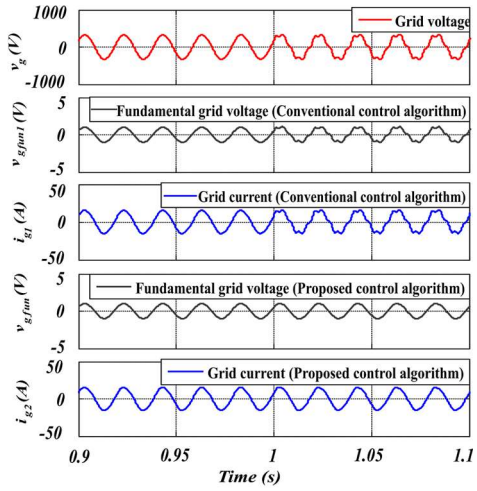

(b)

Fig.12 Comparative response (a) gain margin (GM) and phase margin (PM) of proposed voltage extraction technique (b) grid voltage distortion

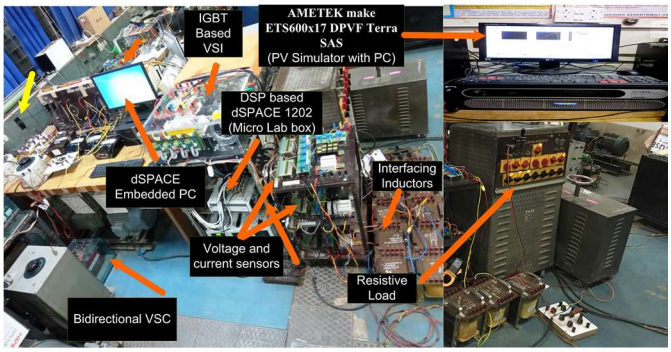

Fig.13 Photograph of the laboratory prototype

A. *MPPT Efficiency Curve*

Figs.14 (a-b) exhibit power tracking efficiency curve of the solar PV array, which is achieved by the P&O MPPT algorithm for a 2.2 kW induction motor feeding a water pump. The P_{pv}-V_{pv} and I_{pv}-V_{pv} curves show that the tracking efficiency is above 99%.

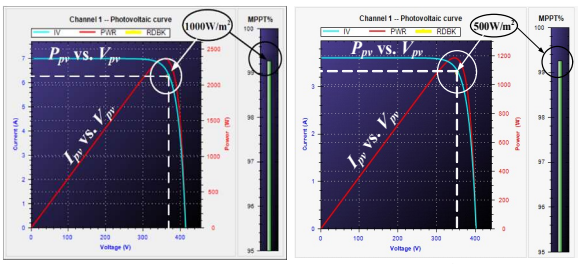

(a) (b)

Fig.14 Tracking performance curve: (a) 1000 W/m² (b) 500 W/m²

B. *Transient Response of System: Change in Insolation*

This system operation during insolation change from 500 W/m² to 1000 W/m² and vice versa, is demonstrated in Figs.15 (a-b). Test results obtained manifest that, in any case, the system operates at its rated condition. During the partial insolation condition, the utility grid provides the remaining power to operate the pump at rated condition. As soon as insolation is restored to its rated value, the motor-pump assembly draws its total power from PV array and therefore, the power extracted from the grid is almost zero.

C. *Condition Pertaining to Grid Operating Pump*

Fig.16 (a) presents the response of the system being operated by single-phase grid alone when the PV generation is unavailable.

During this time, PV array current (I_{pv}) is zero. The satisfactory performance is observed by system variables like grid voltage (v_g), grid current (i_g), motor current (i_a) and rotor speed (ω_m).

Fig.16 (b) exhibits the extreme condition when solar insolation is reduced from the rated condition of 1000 W/m^2 to zero. It is observed from the figure that in this case the rated power is supplied by the grid only. Therefore, a significant rise in the grid current is observed, which is again reduced to zero, when the rated insolation is applied. Fig.16 (c) shows the suitability of the drive when insolation is increased from 400 W/m^2 to 800 W/m^2.

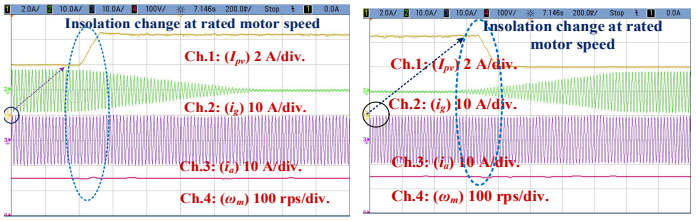

(a) (b)

Fig.15 Dynamic performances of the integrated system (a) (500-1000) W/m^2 (b) (1000-500) W/m^2

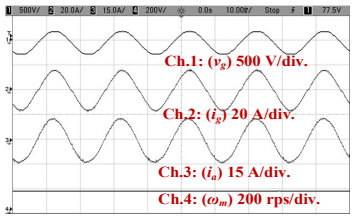

(a)

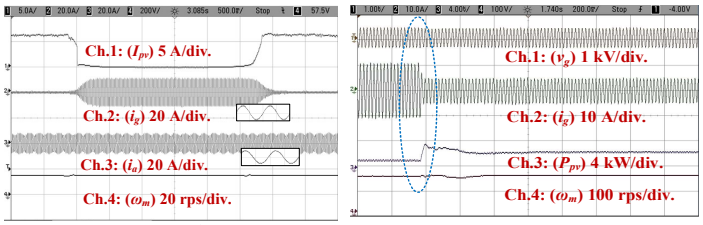

(b) (c)

Fig.16 System performance (a) operated by the grid at rated condition (b) dynamic response of proposed system with integrated sources: (1000-0) W/m^2 and vice versa (c) insolation increased (400-800) W/m^2

D. Dynamic Behavior of Drive System: Speed Change

As it is shown in Figs.17 (a-b), the power provided by the PV array is fed to the utility, when the motor-pump speed is decreased from 150 rad/s to 100 rad/s. In this case, the loading is also decreased. Hence, the remaining power is delivered to the utility grid. The grid voltage (v_g) and grid current (i_g) are 180^0 phase apart, as shown in these figures. Fig.17 (b) shows the speed change from 50 rad/s to 100 rad/s. It is observed from the waveforms that whenever the extra power is transferred to the grid, v_g and i_g are out of phase.

E. Current Reconstruction

Figs.18 (a-c) show test results of motor phase currents reconstruction during starting and during steady-state at the rated condition and 500 W/m^2. The waveforms show that the estimated currents and the measured currents are in phase with same amplitude, which show the current estimation technique is perfectly estimating the phase currents.

F. Comparative Analysis of System under Utility Grid Distortion Condition

Figs.19 (a-b) show operation of PV-grid fed system under grid distortion condition with conventional and new bidirectional power flow control techniques, respectively. The system is operated under reduced insolation. Therefore, the rest of the power is injected from the grid. As it is evident from Fig.19 (a), grid voltage distortion is clearly reflected in the grid current as well as the motor current. When the similar test is performed with this new power flow control, as shown in Fig.19 (b), the distortion in grid voltage (v_g) is not reflected in the grid current and also the motor current is observed to be smoother than the previous case.

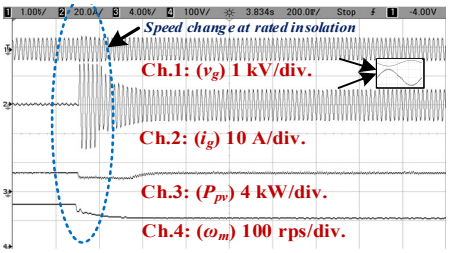

(a)

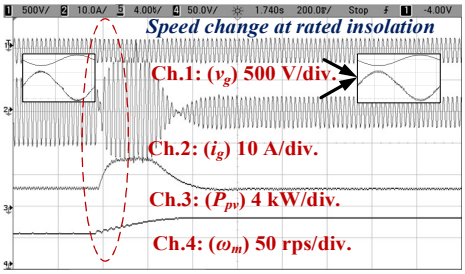

(b)

Fig.17 Dynamic performance during speed change with both the sources together: (a) (150-100) rad/s (b) (50-100) rad/s

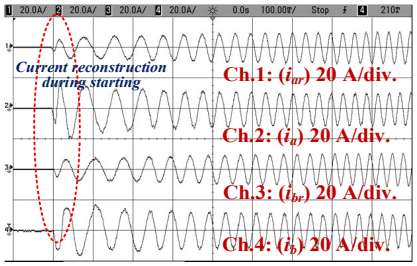

(a)

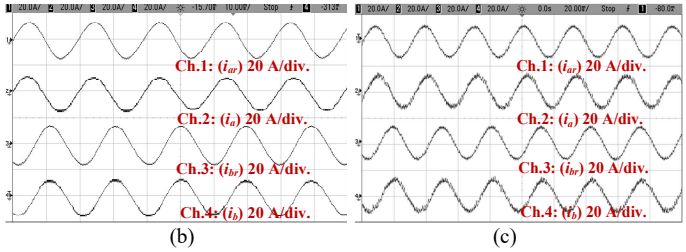

(b) (c)

Fig.18 Current estimation for two phases at (a) starting at rated condition (b) 150 rad/s (c) 100 rad/s

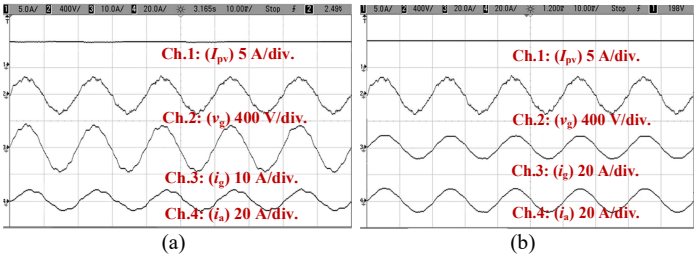

(a) (b)

Fig.19 Comparative analysis under grid voltage distortion condition (a) conventional control technique (b) new control technique

This article has been accepted for publication in a future issue of this journal, but has not been fully edited. Content may change prior to final publication. Citation information: DOI 10.1109/TPEL.2020.2990833, IEEE Transactions on Power Electronics

G. System Performance under Grid Imbalance

Figs.20 (a-b) demonstrate the comparative performances of improved control technique with the conventional generalized based integrator technique. The performance under voltage imbalance in single phase grid fed system is justified by introducing the 10% voltage swell in the grid voltage in both the cases. The reference weight factor of grid current (i_{wref}) is observed to be decreased, which subsequently decreases the grid current in both the cases. This maintains a constant power flow to the motor. Therefore, the motor operates with the constant rated speed delivering rated volume of water through the pump. As soon as the normal condition is restored, the grid voltage restores its nominal value, the weight factor of grid current (i_{wref}) quickly resumes its normal status and so does the grid current (i_g). However, the performance is little bit sluggish when this operation is performed with the existing generalized integrator-based control technique. Therefore, the performances has been captured at high resolution time of 500 ms in Fig.20 (a), whereas it has been captured on 200 ms/div. in Fig.20 (b). This shows the speed of response is faster with the improved control technique. Various indices in Fig.20 show that a fast speed of response has been observed during voltage swell condition and restoration of voltage.

H. Harmonic Spectrum Analysis of Grid Current

The utility is feeding the pump, which has the characteristics of unity power factor with grid voltage and current (v_g and i_g) are in the same phase, as shown in Figs.21 (a-b). The reverse case is observed when the power is fed back to the grid with v_g and i_g is phase displaced by 180^0, as shown in Figs.21 (c-d). However, extra power is made to flow to the grid by reducing pump speed. It can be noticed that in every case, the grid current total harmonics distortion (THD_i) is within 5% and it follows the IEEE-519 standard [29-30].

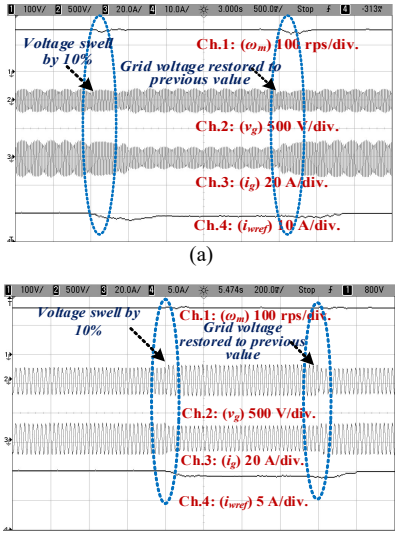

Fig.20 Performance during voltage swell (a) conventional control technique (b) improved control technique

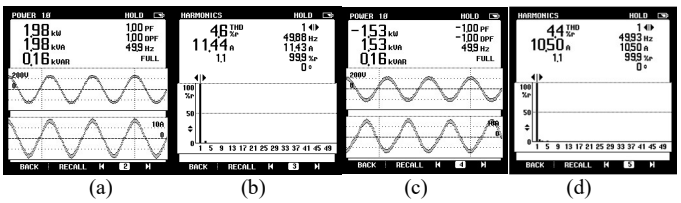

Fig.21 Total harmonic distortion and power factor of utility current (i_g) when (a-b) water pump fed by utility grid alone (c-d) PV array feeds power to grid when speed is reduced

VIII. Conclusions

This new topology with bidirectional power transfer between the single-stage PV array and the grid has been modeled and implemented. The specialty of the system is attributed in its simple power transfer capability in both the direction with an improved third-order integrator based algorithm for voltage template generation, which is insensitive to abnormalities in the grid voltage. The mechanical sensorless control with additional feed-forward flux loop has been used for its better performance in entire speed range for submersible pump, reduced number of sensors and complete utilization of pump. The speed control of the drive and the current reconstruction have been implemented by improved SVM technique. The rearrangement of voltage vector sequences, without insertion of extra vectors, could reconstruct the current at the corner of each sector. In addition, the grid parameters obey the IEEE-519 standard of power quality performance. This new technique with a PV array provides a practical solution for electricity generation and economic liberty for the consumer through the sale of electricity.

Acknowledgment

The authors thank for the financial assistance from MHRD and industry partner Shakti Pumps (India) Ltd. along with JC Bose scholarship Grant to encourage the project work with Grant Number: RP03222G and RP03128, respectively.

Appendices

A. PV Array (Simulated Design Values for One Module)

V_{oc}=21.6 V, V_{mp}=17.8 V, I_{sc}=0.64 A, I_{mp}=0.58 A, P_{mp}=10.3 W.

B. PV Array

V_{oc}=385 V, V_{mp}=345 V, I_{sc}=7.2 A, I_{mp}=6.90 A.

C. IMD Parameters

3 hp, 3-phase, 230 V, 1420 rpm, R_s=0.602Ω, R_r = 0.70 Ω, X_{ls}=X_{lr}=0.95613 Ω, L_m=23.56 Ω, J=0.011Kg-m^2, K_{sv}=0.2, K_{dc}= 0.000638.

D. Parameters Tuning For ITOI

Fig.22 shows the pole-zero plot for selecting K_2. Parameter K_2 is varied from 0 to 5 and it is observed that stable zone lies between 1 and 2, as the conjugate poles move towards imaginary axes. So, the optimized and selected value of K_2 is 1.77 for this work.

E. Comparative Cost Analysis

Table III shows the cost comparison table of this system with the existing systems. It has been found that even the proposed system has merits more than any of the reported topology. It is cheap and reliable system.

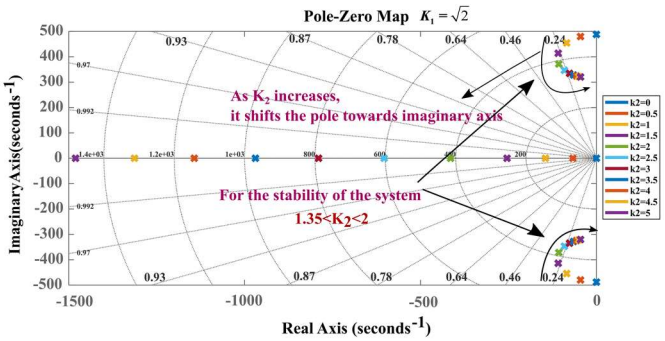

Fig.22 Pole-zero plot to find optimum values of K_1 and K_2

TABLE III COST COMPARISON OF PROPOSED SYSTEM WITH EXISTING SYSTEMS

Devices/ Equipment	Bidirectional Grid Interactive Scalar (*V/f*) Control of PV Fed Induction Motor water Pumping System		Unidirectional Grid Interactive Scalar (*V/f*) Control of PV Fed Induction Motor Water Pumping System [14]	Proposed Bidirectional Single Phase Grid Interactive Single-Stage PV Fed System
	Three Phase Two Stage System	Single Phase Two Stage System		
PWM pulses for controller	13	11	7	10
Voltage sensors (LV 25-P)	3 ($ 180.00)	2 ($ 120.00)	2 ($ 120.00)	2 ($ 120.00)
Current sensors (LA 55-P)	3 ($ 144.75)	2 ($ 96.50)	2 ($ 96.50)	2 ($ 96.50)
DC link capacitor (2700 μF (M), 400V)	1 ($ 19.00)	1 ($ 19.00)	1 ($ 19.00)	1 ($ 19.00)
Boost Converter Inductor (DLFL-0147–12D5)	1 ($ 29.70)	1 ($ 29.70)	1 ($ 29.70)	NA
Semiconductor switches (IGBTs) SKM50GB12V	13 ($ 504.80)	11 ($ 427.16)	7 ($ 271.82)	10 ($ 388.32)
Single-Phase Diode Bridge Rectifier (BSPR 25) (1000V, 25A)	NA	NA	1 ($ 9.57)	NA
Driver circuit (SKYPER 42-R)	($ 214.66)	($ 184.00)	($ 122.66)	($ 153.33)
TOTAL	**$ 1092.91**	**$ 876.36**	**$ 669.25**	**$ 777.15**

REFERENCES

[1] A. K. Bhattacharjee, N. Kutkut and I. Batarseh, "Review of Multiport Converters for Solar and Energy Storage Integration," *IEEE Trans. Power Electron.*, vol. 34, no. 2, pp. 1431-1445, Feb. 2019.

[2] B. P. R. Baddipadiga, V. A. K. Prabhala and M. Ferdowsi, "A Family of High-Voltage-Gain DC–DC Converters Based on a Generalized Structure," *IEEE Trans. Power Electron.*, vol. 33, no. 10, pp. 8399-8411, Oct. 2018.

[3] S. Shukla and B. Singh, "Reduced-Sensor-Based PV Array-Fed Direct Torque Control Induction Motor Drive for Water Pumping," *IEEE Trans. Power Electron.*, vol. 34, no. 6, pp. 5400-5415, June 2019.

[4] K. Lee, W. Yao, C. Bin, Z. Lu, A. Yu and D. Li, "A new oscillation controller design and induction machine stability analysis of volts/Hz based industrial adjustable speed drives," *in Proc. IEEE Energy Conversion Congress and Exposition*, Denver, CO, 2013, pp. 3742-3748.

[5] W. Xu, Y. Jiang, C. Mu and F. Blaabjerg, "Improved Nonlinear Flux Observer-Based Second-Order SOIFO for PMSM Sensorless Control," *IEEE Trans. Power Electron.*, vol. 34, no. 1, pp. 565-579, Jan. 2019.

[6] B. Singh, S. Kumar and C. Jain, "Damped-SOGI-Based Control Algorithm for Solar PV Power Generating System," *IEEE Trans. Ind. Appl.*, vol. 53, no. 3, pp. 1780-1788, May-June 2017.

[7] Y. Jiang, W. Xu, C. Mu, J. Zhu and R. Dian, "An Improved Third-Order Generalized Integral Flux Observer for Sensorless Drive of PMSMs," *IEEE Trans. Ind. Electron.*, vol. 66, no. 12, pp. 9149-9160, Dec. 2019.

[8] Z. Xin, X. Wang, Z. Qin, M. Lu, P. C. Loh and F. Blaabjerg, "An Improved Second-Order Generalized Integrator Based Quadrature Signal Generator," *IEEE Trans. Power Electron.*, vol. 31, no. 12, pp. 8068-8073, Dec. 2016.

[9] A. Pal, S. Das, and A. K. Chattopadhyay, "An improved rotor flux space vector based MRAS for field-oriented control of induction motor drives," *IEEE Trans. Power Electron.*, vol. 33, no. 6, pp. 5131–5141, June 2018.

[10] F. F. M. El-Sousy, "Adaptive dynamic sliding-mode control system using recurrent RBFN for high-performance induction motor servo drive," *IEEE Trans. Ind. Info.*, vol. 9, no. 4, pp. 1922–1936, Nov 2013.

[11] P. Shah and B. Singh, "Kalman Filtering Technique for Rooftop-PV System Under Abnormal Grid Conditions," *IEEE Trans. Sustain. Energy*, vol. 11, no. 1, pp. 282-293, Jan. 2020.

[12] S. Maiti, V. Verma, C. Chakraborty, and Y. Hori, "An adaptive speed sensorless induction motor drive with artificial neural network for stability enhancement," *IEEE Trans. Ind. Inf.*, vol. 8, no. 4, pp. 757–766, Nov 2012.

[13] J. Kiviluoma, S. Heinen, H. Qazi, H. Madsen, G. Strbac, C. Kang, N. Zhang, D. Patteeuw, and T. Naegler, "Harnessing flexibility from hot and cold: Heat storage and hybrid systems can play a major role," *IEEE Power and Energy Magazine*, vol. 15, no. 1, pp. 25–33, Jan 2017.

[14] U. Sharma, B. Singh and S. Kumar, "Intelligent grid interfaced solar water pumping system," *IET Renew. Power Gener.*, vol. 11, no. 5, pp. 614-624, 2017.

[15] S. Murshid and B. Singh, "Analysis and Control of Weak Grid Interfaced Autonomous Solar Water Pumping System for Industrial and Commercial Applications," *IEEE Trans. Ind. Appl.*, vol. 55, no. 6, pp. 7207-7218, Nov.-Dec. 2019.

[16] R. Kumar and B. Singh, "Brushless DC motor-driven grid-interfaced solar water pumping system," *IET Power Electron.*, vol. 11, no. 12, pp. 1875-1885, 2018.

[17] B. Singh and S. Murshid, "A grid-interactive permanent-magnet synchronous motor-driven solar water-pumping system," *IEEE Trans. Ind. Appl.*, vol. 54, no. 5, pp. 5549–5561, Sept 2018.

[18] H. A. Sher, A. F. Murtaza, A. Noman, K. E. Addoweesh, K. Al-Haddad and M. Chiaberge, "A New Sensorless Hybrid MPPT Algorithm Based on Fractional Short-Circuit Current Measurement and P&O MPPT," *IEEE Trans. Sustain. Energy*, vol. 6, no. 4, pp. 1426-1434, Oct. 2015.

[19] R. Kumar and B. Singh, "Grid interfaced solar PV based water pumping using brushless dc motor drive," *in Proc. IEEE Int. Confer. Power Electron., Drives and Energy Sys.* (*PEDES*), Dec 2016, pp. 1–6.

[20] M. Ciobotaru, R. Teodorescu, and V. G. Agelidis, "Offset rejection for PLL based synchronization in grid-connected converters," *in Proc. Annual IEEE Applied Power Electron. Conf. and Expo.*, Feb 2008, pp. 1611–1617.

[21] H. Li, A. Monti, and F. Ponci, "A fuzzy-based sensor validation strategy for AC motor drives," *IEEE Trans. Ind. Inf.*, vol. 8, no. 4, pp. 839–848, Nov 2012.

[22] B. Hafez, A. S. Abdel-Khalik, A. M. Massoud, S. Ahmed and R. D. Lorenz, "Single-Sensor-Based Three-Phase Permanent-Magnet Synchronous Motor Drive System With Luenberger Observers for Motor Line Current Reconstruction," *IEEE Trans. Ind. Appl.*, vol. 50, no. 4, pp. 2602-2613, July-Aug. 2014.

[23] J. I. Ha, "Voltage injection method for three-phase current reconstruction in PWM inverters using a single sensor," *IEEE Trans. Power Electron.*, vol. 24, no. 3, pp. 767–775, March 2009.

[24] V. Vlatkovic, D. Borojevic, and F. C. Lee, "Input filter design for power factor correction circuits," *IEEE Trans. Power Electron.*, vol. 11, no. 1, pp. 199–205, Jan 1996.

[25] Peter Vas, Sensorless vector and direct torque control, Oxford University Press, Oxford Science Publications, Inc. 1998, pp. 464-465.

[26] C. Lv, Y. Xing, J. Zhang, X. Na, Y. Li, T. Liu, D. Cao, and F. Wang, "Levenberg-marquardt backpropagation training of multilayer neural networks for state estimation of a safety-critical cyber-physical system," *IEEE Trans. Ind. Inf.,* vol. 14, no. 8, pp. 3436–3446, Aug 2018.

[27] J. Ahmed and Z. Salam, "A modified P&O maximum power point tracking method with reduced steady-state oscillation and improved tracking efficiency," *IEEE Trans. Sustain. Energy*, vol. 7, no. 4, pp. 1506–1515, Oct 2016.

[28] J. Ahmed and Z. Salam, "An Enhanced Adaptive P&O MPPT for Fast and Efficient Tracking Under Varying Environmental Conditions," *IEEE Trans. Sustain. Energy*, vol. 9, no. 3, pp. 1487-1496, July 2018.

[29] "IEEE recommended practices and requirements for harmonic control in electrical power systems," *IEEE Std*. 519-1992, pp. 1–112, April 1993.

[30] G. W. Chang, Chia-Ming Yeh and Wei-Cheng Chen, "Meeting IEEE-519 current harmonics and power factor constraints with a three-phase three-wire active power filter under distorted source voltages," *IEEE Trans. Power Delivery*, vol. 21, no. 3, pp. 1648-1654, July 2006.

Saurabh Shukla was born in Andal (W.B), India, in 1988. He received the B.Tech. degree in Electrical Engineering from Asansol Engineering College (WBUT) in 2010, Post Graduate Diploma Course in Thermal Power Plant Enginnering from National Power Training Institute (N.P.T.I) Nangal in 2012 and M.Tech. degree in Instrumentation and Control Enginnering from the Sant Longowal Institute of Engineering and Technology (SLIET) Sangrur, Punjab in 2014. He has been awarded the Ph.D. degree in the Department of Electrical Engineering, Indian Institute of Technology Delhi in 2019. His areas of research interests include power electronics, electrical machines and drives, and renewable energy.

Bhim Singh (SM'99, F'10) was born in Rahamapur, Bijnor (UP), India, in 1956. He has received his B.E. (Electrical) from the University of Roorkee (Now IIT Roorkee), India, in 1977 and his M.Tech. (Power Apparatus & Systems) and Ph.D. from the IIT Delhi, India, in 1979 and 1983, respectively. In 1983, he joined the Department of Electrical Engineering, University of Roorkee, as a Lecturer. He became a Reader there in 1988. In December 1990, he joined the Department of Electrical Engineering, IIT Delhi, India, as an Assistant Professor, where he has become an Associate Professor in 1994 and a Professor in 1997. He has been Head of the Department of Electrical Engineering at IIT Delhi from July 2014 to August 2016. He has been Dean, Academics at IIT Delhi , August 2016 to August 2019. He is J. C. Bose Fellow of DST, Government of India since December 2015. He is CEA Chair Professor since January 2019. Prof. Singh has guided 83 Ph.D. dissertations, and 167 M.E./M.Tech./M.S.(R) theses. He has been filed 52 patents. He has executed more than eighty sponsored and consultancy projects. His areas of interest include solar PV grid interface systems, microgrids, power quality monitoring and mitigation, solar PV water pumping systems, improved power quality AC-DC converters.